

Kalman Filter Estimation of Rotor-State Flapping: An Optimization-based Approach with UH-60 Flight Test Data

Marit E. Knapp
Student Researcher
Santa Clara University & San Jose State
University Research Foundation
Santa Clara & Moffett Field, CA

Christina M. Ivler
Marcos G. Berrios*
Tom Berger
Mark B. Tischler‡
Aerospace Engineers
Aviation Development Directorate
AMRDEC, U.S. Army
Moffett Field, CA

ABSTRACT

Flight testing of explicit rotor-state feedback (RSF) fly-by-wire control laws showed that measuring rotor tip-path-plane (TPP) flapping, via a laser measurement system, provided additional lead to the control system. This resulted in superior handling qualities in turbulence and heavy winds and improved stability margins. However, a significant impediment to the adoption of explicitly measured RSF has been the difficulty in extracting reliable rotor measurements. Therefore, this paper describes the development of a Kalman filter that was designed to estimate rotor TPP coordinates, and remove noise from the flapping signals while retaining the useful information without introducing large time delay, as would be the case for conventional low pass filtering. A new method for the design of the process noise covariance matrix using optimization of frequency domain specifications was implemented using flight test data from the UH-60 Black Hawk. The design was integrated into an explicit rotor-state feedback control algorithm, where it was tested for robustness to sensor faults and effectiveness based on improvements to stability margins. The results showed that the Kalman filter was robust to rotor blade sensor spike and drop-out faults and resulted in improved stability margins and handling qualities.

NOTATION

u, v, w	Roll, pitch, yaw angular velocities	K	Kalman gain
p, q, r	Roll and pitch angular accelerations	Q, R	Process, measurement noise covariance matrices
X, Y	Longitudinal and lateral position	P	Estimation error covariance matrix
v_x, v_y, v_z	North, east, down ground speeds	k	Time step
β_{ls}	Lateral flapping (body frame)	\sim	Superscript denoting measurement
β_{lc}	Longitudinal flapping (body frame)	\wedge	Superscript denoting estimate
β_i	Individual blade flapping (rotating frame)	ω	Frequency (rad/s)
$\delta_{lat}, \delta_{lon}$	Longitudinal and lateral pilot inputs	σ	Standard deviation
$\delta_{col}, \delta_{ped}$	Collective and pedal pilot inputs	Δ	Optimization design parameter
θ, ϕ	Roll, pitch attitudes	eRSF	Explicit RSF control laws
ψ	Azimuth angle of rotor	RSF	Rotor-state feedback
x, u, y	State, input, output vectors	KF	Kalman Filter
w, v	Process, measurement noise vectors	KFa	Kalman filter design a
A, B, C, D	State space matrices	KFb	Kalman filter design b
		TPP	Tip-path-plane
		SNR	Signal-to-noise ratio
		FDEE	Frequency domain estimation error
		ω_{DRB}	Disturbance rejection bandwidth
		ω_c	0 dB broken loop crossover frequency

Presented at the AHS 73rd Annual Forum, Fort Worth, Texas, USA, May 9-11, 2017. This is a work of the U.S. Government and not subject to copyright in the U.S. Approved for public release: Distribution is unlimited.

*Aerospace Engineer, operational Air Force pilot
‡Flight Control Technology Group Lead, Senior Scientist

INTRODUCTION

The use of rotor tip-path-plane (TPP) flapping motions has been shown in flight testing and simulation to improve helicopter ride quality in gusty conditions and decrease pilot workload during precision maneuvers performed in adverse weather [1, 2, 3, 4]. Flight testing of the rotor-state feedback (RSF) fly-by-wire control laws on board the Rotorcraft Aircrew Systems Concepts Airborne Laboratory (RASCAL) JH-60A aircraft [5] showed that using RSF in the control algorithm provided additional lead to the control system, which resulted in superior handling qualities in turbulence and heavy winds, while maintaining sufficient stability margins, compared to standard fuselage feedback [2]. Flight tests indicated that RSF using explicitly measured rotor states (eRSF), increases phase margin which allowed for higher disturbance rejection bandwidth (DRB) and crossover frequency (ω_c), which results in improved tracking performance in flight on the order of 10-50% for most ADS-33E-PRF Mission Task Elements [2]. In addition to using rotor TPP motion for feedback, accurate and reliable measurements are also desirable to improve rotorcraft simulation models, identify correlation with acoustic measurements and noise estimation, enable individual blade control, and provide vehicle health monitoring during flight tests [6, 7]. The Future Vertical Lift fleet will likely be equipped with blade mounted sensors for real-time acquisition of main rotor motions [8]. However, a significant impediment to the adoption of eRSF remains the difficulty in extracting reliable rotor response measurements [9].

Measurement of rotor states is typically performed in the rotating frame, with sensors measuring blade flapping, lead-lag, and pitch motion. However, control laws are applied to the swashplate in the nonrotating frame, necessitating the conversion of rotor states from the rotating to nonrotating frame, or individual blade flapping to TPP attitude [10]. The TPP coordinates describe the circular path formed by the tips of blades with lateral and longitudinal flapping at a coning angle, as shown in Figure 1 [11, 12]. Rotor TPP measurements, derived through the multi-blade coordinate transformation of individual rotor blade flapping measurements, can contain a considerable amount of noise and are sensitive to environmental conditions. To include blade flapping measurements in RSF,

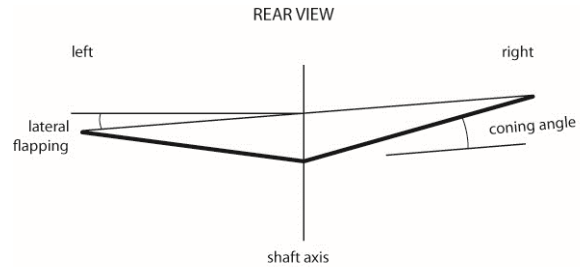


Figure 1. Lateral flapping, β_{1s} tip-path-plane tilt [12].

conventional filtering techniques are generally employed, which introduce significant time delay [13]. Additionally, the increased complexity of the blade measurement system can deliver intermittent and spurious TPP coordinate data to the RSF control algorithm.

While there have been few flight tests of RSF systems, researchers have investigated methods to process and utilize rotor blade flapping measurements for feedback in control law algorithms. Theoretical and experimental results show that an estimator, particularly the Kalman filter (KF), can be used to resolve robust and reliable rotor response measurements in real-time [14, 15]. A KF, also known as a linear quadratic estimator, is an adapted state estimator, which fuses measurement data from multiple sensors and uses a mathematical model based on physical laws or system identification to predict the dynamic behavior of the system [16]. The KF refines state estimates through an innovation step that minimizes the variance of the estimation error (i.e., the difference between the estimated output and the raw output) which are typically due to uncertainties in the mathematical model and noisy measurements [16]. In the KF algorithm, the measurement and process noise covariance matrices, \mathbf{R} and \mathbf{Q} , respectively, play an important role in determining the Kalman gain, and therefore the bandwidth and stability of the filter [17].

Generally, filter parameters are tuned off-line using simulated data and are subsequently used for on-line, real-time processing [18]. Setting the covariance matrices, \mathbf{R} and \mathbf{Q} , is a difficult task because process uncertainties and noise affecting output measurements are unknown; tuning strategies range from simple manual ad-hoc or trial-and-error methods to complex, computationally time-intensive methods such as those explored in Ref. [19, 20, 21].

Approaches such as autocovariance least-squares method and Bayesian approach using Monte Carlo simulations take numerous iterations and are based on time-domain performance. Nonetheless, the industrial standard still relies on semi-empirical tuning and diagonal parameterization of \mathbf{R} and \mathbf{Q} .

The objective of this research was to design a KF to estimate rotor TPP coordinates, remove noise from the flapping signals while retaining the useful information, without introducing large time delay. A new method for the tuning of the \mathbf{Q} matrix using flight data and direct optimization of frequency domain specifications was implemented. The KF designs were tested for their robustness to sensor faults and effectiveness based on improvements to stability margins after integration into the eRSF control system, and flown in a fixed base simulator [1, 2].

COLLECTION OF FLIGHT TEST DATA

Many technologies for measuring blade flapping motion have been explored, including strain gauges, blade-mounted pressure transducers, accelerometers, Hall-effect, magneto-inductive and Eddy current distance sensors, ultrasonic transducers, optical blade position measurement and vision systems [9, 7, 22]. This research uses flight test data collected with a rotor blade measurement system on the RASCAL UH-60 Black Hawk in 2010 and 2015-2016 [2]. Flight test data from 40 records, which includes ADS-33E Mission Task Elements (MTEs) [23], frequency sweeps, and hovering in simulated and actual turbulence, were used to evaluate and optimize the performance of the KF. The rotor blade measurement system on RASCAL



Figure 2. Rotor blade measurement system [12].

consists of laser distance transducers and azimuth encoder shown in Figure 2 [13].

The laser measurement system is mounted on the rotor in the rotating frame in order to measure flap, lead-lag, and pitch blade angles on each of the four blades [6]. Signals and power pass between the rotating and fixed frames through a slip-ring [24]. The flap, lead-lag, and pitch blade angles of an individual blade are used to calculate a calibrated flap angle, β_i , for the blade. Then, the multi-blade coordinate transform converts the calibrated flap angles of each blade, β_i , and a separate rotor-azimuth measurement, ψ , to the tip-path plane (TPP) longitudinal and lateral flapping angles, β_{1c} and β_{1s} [25]:

$$\beta_{1c} = \frac{1}{2} \left[\beta_1 \cos(\psi) + \beta_2 \cos\left(\psi + \frac{\pi}{2}\right) + \beta_3 \cos(\psi + \pi) + \beta_4 \cos\left(\psi + \frac{3\pi}{2}\right) \right], \quad (1)$$

$$\beta_{1s} = \frac{1}{2} \left[\beta_1 \sin(\psi) + \beta_2 \sin\left(\psi + \frac{\pi}{2}\right) + \beta_3 \sin(\psi + \pi) + \beta_4 \sin\left(\psi + \frac{3\pi}{2}\right) \right]. \quad (2)$$

From Equations (1) and (2), one can see that errors in blade or azimuth measurements will skew the calculation of the TPP measurement. Reference [2] showed that azimuth angle bias would have a small and likely tolerable increase in cross-coupling (cross-contamination), where lateral motion could be misrepresented in the longitudinal direction, and vice versa. Compounding these potential vulnerabilities, the laser sensors are inherently noisy and sensitive to sunlight, dust, and sand.

In previous flight testing, the eRSF control laws integrated conventionally filtered blade flapping measurements. Rotor TPP signals were processed with a 5Hz Butterworth filter and two notch filters at 4/rev and 1/rev to mitigate noise [1, 2]. This introduced a time delay of approximately 0.05 seconds, which adds approximately 10 deg of additional phase lag to the crossover frequency thereby limiting performance.

KALMAN FILTER DESIGN

The KF was designed to replace the Butterworth and notch filters, and deliver superior rotor TPP flap angle estimates, with reduced lag to the eRSF control block shown in Figure 3. As shown in Figure 4, a linear model, tested and validated with

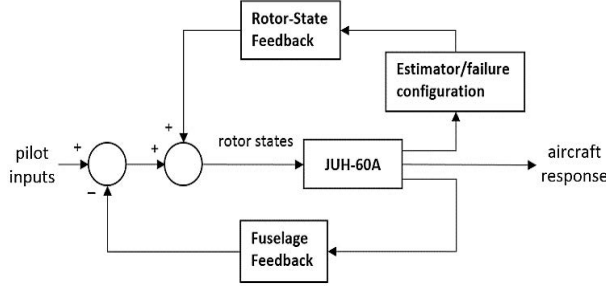


Figure 3. State estimator and failure configuration architecture with eRSF.

actuator inputs, fuselage, and rotor-state measurements from flight data, formed the basis of the KF. The Kalman filter was implemented in the discrete state space form [18]:

$$\begin{aligned} \mathbf{x}_k &= \mathbf{A}\mathbf{x}_{k-1} + \mathbf{B}\mathbf{u}_{k-1} + \mathbf{w}_{k-1} \\ \mathbf{y}_k &= \mathbf{C}\mathbf{x}_k + \mathbf{D}\mathbf{u}_k \end{aligned} \quad (3)$$

where model matrices \mathbf{A} and \mathbf{B} relate the past states and control inputs at $k-1$, to the current state time step k . The value \mathbf{w} represents the process noise, and matrices \mathbf{C} and \mathbf{D} relate the states and inputs to the outputs, \mathbf{y} . The actual measured outputs are described by:

$$\tilde{\mathbf{y}}_k = \mathbf{y}_k + \mathbf{v}_k \quad (4)$$

where measurement noise, \mathbf{v} , is added to the model outputs. The Kalman filter design is based on linear state and measurement dynamics, where process and measurement noise are modeled as independent (of each other) and zero mean, white Gaussian [18]. In reality, the noise may not be perfectly Gaussian; but, in practice, the process and measurement noise, \mathbf{w} and \mathbf{v} , can be modeled as having normal probability distributions, such that their mean values and covariances are determined by the expressions [18]:

$$E[\mathbf{v}(t)] = 0, E[\mathbf{w}(t)] = 0, \quad (5)$$

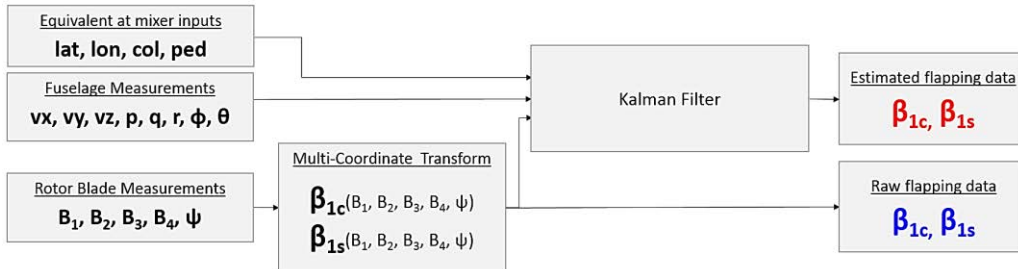


Figure 4. Rotor-state estimation block diagram.

$$E[\mathbf{v}(t)\mathbf{v}^T(t)] = \mathbf{R}, E[\mathbf{w}(t)\mathbf{w}^T(t)] = \mathbf{Q}, \quad (6)$$

with constant process noise covariance matrix \mathbf{Q} and constant measurement noise covariance matrix \mathbf{R} .

The discrete Kalman filter equations use a two-step prediction-correction algorithm. First, the predicted state $\hat{\mathbf{x}}^-$ and error covariance estimates \mathbf{P} are computed by [18]:

$$\hat{\mathbf{x}}_k^- = \mathbf{A}\hat{\mathbf{x}}_{k-1} + \mathbf{B}\mathbf{u}_{k-1}, \quad (7)$$

$$\mathbf{P}_k^- = \mathbf{A}\mathbf{P}_{k-1}\mathbf{A}^T + \mathbf{Q}. \quad (8)$$

Then the correction step generates a posterior state estimate [18]:

$$\hat{\mathbf{x}}_k = \hat{\mathbf{x}}_k^- + \mathbf{K}_k(\tilde{\mathbf{y}}_k - \mathbf{C}\hat{\mathbf{x}}_k^-), \quad (9)$$

with the Kalman gain \mathbf{K} given by [18]:

$$\mathbf{K}_k = \mathbf{P}_k^- \mathbf{C}^T (\mathbf{C}\mathbf{P}_k^- \mathbf{C}^T + \mathbf{R})^{-1}, \quad (10)$$

and updates \mathbf{P} , the error covariance estimate by [18]:

$$\mathbf{P}_k = (\mathbf{I} - \mathbf{K}_k \mathbf{C}) \mathbf{P}_k^-. \quad (11)$$

The Kalman gain is selected to minimize the error covariance of the residual, the difference between the actual measurement and estimated or predicted measurement ($\tilde{\mathbf{y}} - \mathbf{C}\hat{\mathbf{x}}^-$). When the covariance matrices \mathbf{Q} and \mathbf{R} are set to constant values, the estimation error covariance \mathbf{P} and Kalman gain \mathbf{K} will rapidly converge to constant values [18].

If the noise in the system is known or measurable then these values would determine the covariance matrices. However, even if the covariance matrices are measurable, they are often adjusted based on the desired characteristics of the estimates. In cases where actual measurements are trustworthy, the measurement noise covariance, \mathbf{R} can be set very low. Alternatively, when the model is accurate or the measurements are not as trusted,

the process noise covariance \mathbf{Q} will be relatively small. Note that the Kalman filter's performance does not depend on the absolute process and measurement noise covariance matrices, \mathbf{Q} and \mathbf{R} , rather on their ratio [17].

For this application, the linear model was a reduced order version of the FORECAST state-space model of the UH-60 [26]. The model is an eight degree of freedom representation of the aircraft, including 8 fuselage states, 2 rotor states and 4 pilot inceptor inputs. The state variables used in this KF are:

$$\mathbf{x} = [u, v, w, p, q, r, \phi, \theta, \beta_{1c}, \beta_{1s}]^T \quad (12)$$

where: u, v and w are the body velocities, p, q and r are angular velocities, ϕ and θ are Euler angles, and β_{1c} and β_{1s} are (body frame) longitudinal and lateral flapping. The control inputs are:

$$\mathbf{u} = [\delta_{lat}, \delta_{lon}, \delta_{col}, \delta_{ped}]^T \quad (13)$$

where δ_{lat} and δ_{lon} are lateral and longitudinal cyclic stick, δ_{col} is collective stick and δ_{ped} is the pedal input. All of the state variables were measured at a sampling frequency of 320 Hz and down sampled to 64 Hz.

The measurement noise covariance matrix \mathbf{R} was computed using flight data at trim. Covariance values, ρ , were calculated from a culmination of 10 flight records. Measurement noise covariance values specified how each of the measurements interact with each other. Theoretically, cross-correlation values or covariance values between different measurement noises are zero because measurements are independent of each other [18]; in reality, these values are non-zero but small. The covariance matrix is dominated by the diagonal elements, which are equal to the variance of the measurement noise. The stochastic characteristics of the measurements were evaluated in the frequency domain to determine the validity of modeling the noise as Gaussian white noise. The power spectral density of white noise has uniform power over all frequencies. The measurement noise was observed to have nearly constant power, except at 1/rev and 4/rev and over 28 rad/s, where RASCAL is known to have harmonic vibration. For the purpose of this research, the measurement noise was approximated as Gaussian white noise, covariance values were computed in the

time domain. As expected, computation of \mathbf{R} produced very small cross-correlation values between measurements relative to the diagonal auto-correlation values, the variance of the measurement noise. The full measurement noise covariance matrix was used in this study. The dominant, diagonal terms of the \mathbf{R} matrix are presented in Table 1. The \mathbf{R}

Table 1. Measurement noise covariance matrix diagonal terms.

Signal variance	Value (units)
u	$32.9*10^{-3}$ (ft/sec)
v	$28.5*10^{-3}$ (ft/sec)
w	$6.79*10^{-3}$ (ft/sec)
p	$4.26*10^{-4}$ (rad/sec)
q	$1.32*10^{-4}$ (rad/sec)
r	$4.95*10^{-5}$ (rad/sec)
ϕ	$3.42*10^{-5}$ (rad)
θ	$4.43*10^{-5}$ (rad)
β_{1c}	$3.85*10^{-3}$ (rad)
β_{1s}	$4.78*10^{-3}$ (rad)

matrix was adjusted based on the desire to estimate reliable blade flapping and that the blade measurements can be noisy and drop out. The blade flapping measurement noise covariance terms were increased by a factor of 10. This produces estimates of blade motion that rely less on the actual blade measurements, and more on other trusted sensor measurements.

With the \mathbf{R} matrix set, a novel optimization method was used to tune the process noise covariance matrix, \mathbf{Q} . The process noise covariance matrix optimization was initialized with an ad hoc method. By manipulating terms of a diagonal matrix to produce estimates with reduced high frequency noise but, that still captured the lower frequency domain behavior of lateral and longitudinal flapping. This ad hoc \mathbf{Q} was used for initial design specifications and scaling purposes, which are discussed in the following sections.

KALMAN FILTER DESIGN SPECIFICATIONS

A set of frequency domain design specifications were established to optimize the tuning of the KF and produce an overall performance index, which provides the "optimization" criteria for

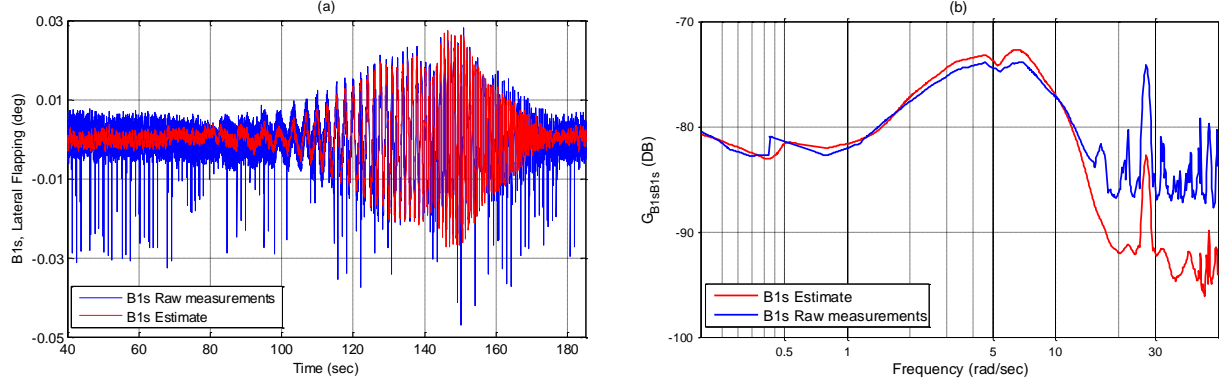


Figure 5. Time and frequency domain responses of lateral flapping angle from a roll frequency sweep maneuver.

the KF design. Typically, KF performance is evaluated by calculating the root mean square (RMS) error of the estimates in the time domain [17, 19]. However, the frequency domain representation is useful for revealing characteristic properties of the signal, especially for signals with cyclic behavior like rotor flapping angles. The same raw and estimated lateral flapping responses are compared in the time and frequency domain in Figure 5 (a) and (b). The time history shows the estimate has less noise than the raw lateral flapping signal, and the frequency domain shows that the signals behave similarly, up to around 16 rad/s, where it is evident that the estimate has much less high frequency content. The frequency domain specifications used to drive the optimization were signal-to-noise ratio (SNR), frequency domain estimator error (FDEE), and time delay. A time domain specification, commanded actuator activity in the RSF implementation, was also checked. The specifications are set to bounds/limits using Reference [12], filtered flapping signal performance, and engineering judgement. These specifications will be described in detail in the following sections.

Signal-to-Noise Ratio

Signal-to-noise ratio (SNR) is the ratio of the power of the meaningful information of the signal and the power of noise mixed in with the signal. Analysis of the power spectral densities of the flapping signals (e.g., Figure 5(b)) reveals the frequency distribution of the measured signal, specifically, the contribution of noise in the measured signal [12]. The SNR of the estimated lateral flapping, for example, was calculated from integrating over the power spectral density of the measurement β_{1s} ($G_{\beta_{1s}\beta_{1s}}$), where the useful information-carrying portion of the measurement,

$\sigma_{\beta_{1s}^2 signal}$, was considered to be between 0.3 to 18 rad/s [12]:

$$\sigma_{\beta_{1s}^2 signal} = \int_{0.3}^{18} G_{\beta_{1s}\beta_{1s}} d\omega \quad (14)$$

and the noise in the measurement, $\sigma_{\beta_{1s}^2 noise}$, was considered to be distributed between 18 rad/s and 1/5 the sampling frequency, f_s :

$$\sigma_{\beta_{1s}^2 noise} = \int_{18}^{2\pi f_s/5} G_{\beta_{1s}\beta_{1s}} d\omega. \quad (15)$$

The signal-to-noise was calculated with:

$$SNR = \sigma_{signal} / \sigma_{noise}. \quad (16)$$

The lateral TPP flapping has a SNR of approximately 2.4 when it was measured directly and 9.6 when processed with the Butterworth and notch filters, previously used for eRSF. This filtration method comes at the cost of significant time delay (0.05 sec) that degrades RSF performance.

Frequency Domain Estimation Error (FDEE)

It was important to measure how closely the KF estimates were representative of the lower-order dynamics of the raw measured signals, because the sensors were shown to produce accurate data below 18 rad/s [2]. The FDEE between the estimated and raw measurement frequency responses, $T(\omega)_{est}$ and $T(\omega)_{actual}$, is measured where the meaningful dynamic characteristics occur, between the frequency range ω_{min} and ω_{max} (typically around 0.3 to 18 rad/s) [12]:

$$FDEE = \sum_{\omega_{min}}^{\omega_{max}} [(|T(\omega)_{est}| - |T(\omega)_{raw}|)^2 + 0.0175 * (\angle T(\omega)_{est} - \angle T(\omega)_{raw})^2], \quad (17)$$

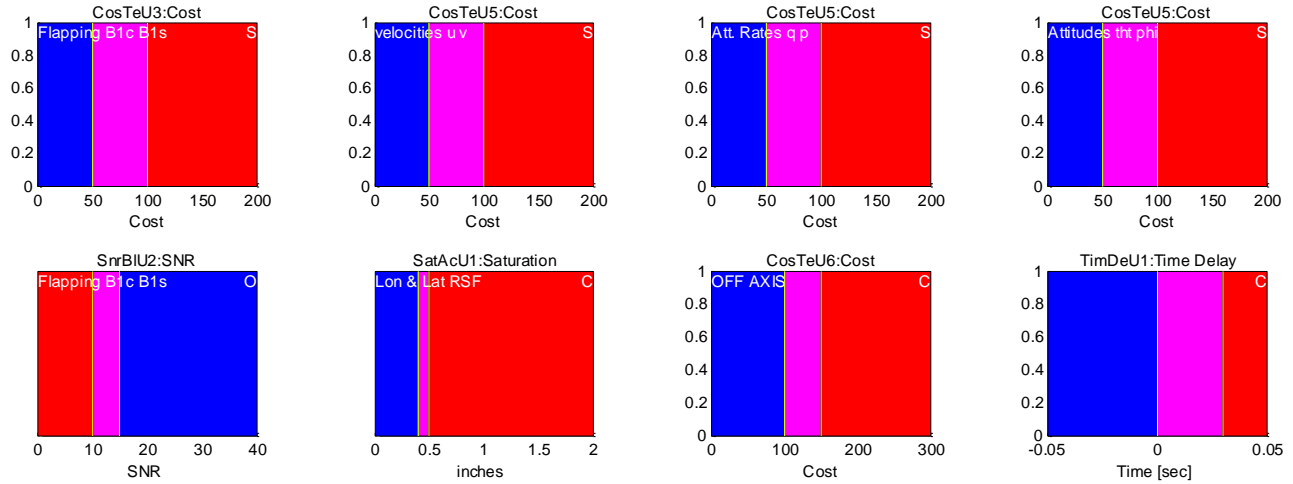


Figure 6. Setup of Kalman filter design specifications for optimization in CONDUIT®.

Table 2 . Optimization Specifications.

Constraint Type	Specmaker Name	Design Parameter	Description	Boundary (excellent, acceptable)
Constraint (CONDUIT® Soft)	CosTeU3	Flapping FDEE	Estimated signal error Equ. 17	0-50, 50-100
	CosTeU5	on-axis FDEE	Estimated signal error Equ. 17	0-50, 50-100
Objective	SnrBIU2	flapping SNR	Estimated signal SNR Equ. 16	15-above, 10-15
	TimDeU1	Time delay	Time delay in estimated signal	0, 0-0.03
Check Only	SatAcU1	Actuator activity	Actuator saturation level	-0.4-0.4, -0.5-0.5
	CosTeU6	Off-axis FDEE	Estimated signal error Equ. 17	0-100, 100-150

CONDUIT®. A sensitivity analysis for insensitivities and Cramér-Rao bounds of the design parameters ensured the problem was well posed, and reduces the likelihood that a local minima was reached [12]. For this design, the optimization will meet all the FDEEs constraints, and maximize the SNR of the flapping signals. Time delay and commanded actuator activity were checked, but did not drive the optimization. The required lateral and longitudinal flapping FDEE was incrementally tightened and re-optimized in a design margin optimization [27] to produce a family of optimized Q matrices, all optimized solutions for the KF designs.

KALMAN FILTER DESIGN TRADE-OFFS

Important trade-offs were highlighted from the family of KF designs that were determined via design margin optimization. Figure 7 shows the trade-off between SNR and FDEE for the family of optimized solutions, as indicated by the red traces. This key trade-off shows that SNR can be improved (increased) only when the frequency domain

estimation error degrades (increases). This is due to the nature of forming state estimates based on measurements and a mathematical model. Relying more on the model, which is accurate but not identical to flight data, results in a better SNR but reduced accuracy of flapping signal, shown in increased FDEE. A knee in the curve occurs at around a FDEE of 80, indicating the trade-off

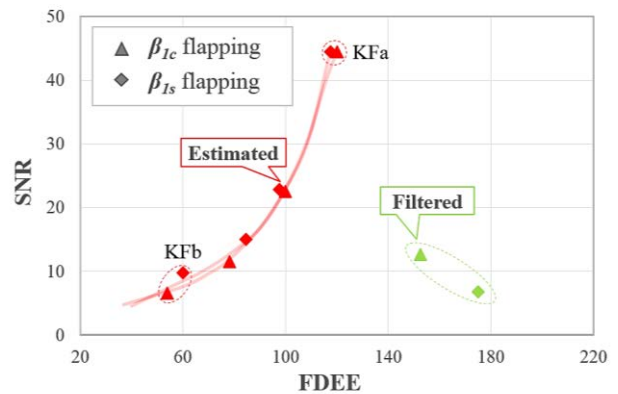


Figure 7. SNR and FDEE trade-off.

becomes more sensitive after this point. The conventional filtering method can be seen in green in Figure 7. Notably, the filtered flapping signals had approximately 0.05 seconds of added time delay, reflected in the large FDEEs, while estimated flapping signals had little to no time delay.

To test the robustness of the KF designs, the effect and severity on commanded actuator activity during the worst-case fault scenarios were evaluated. The most dangerous faults were evaluated based on flight data. The worst-case fault scenario occurred when opposing blade laser sensors saturated with spikes and drop outs; this could cause the estimated flapping signals to produce large, undesirable and spurious, commanded actuator inputs to the RSF. Figure 8 shows how severe faults affect flapping,

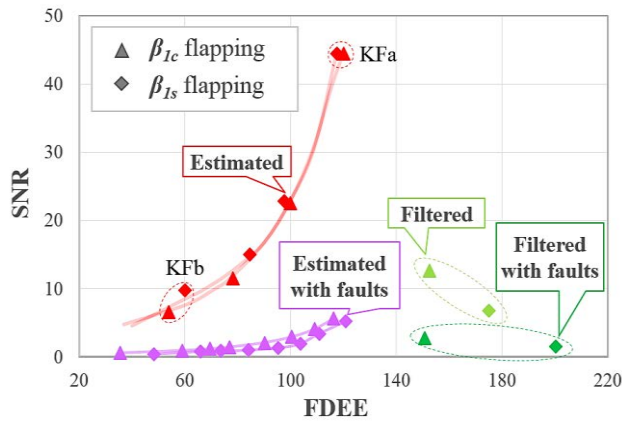


Figure 8. SNR and FDEE trade-off with faults.

where injected faults caused the SNR of the estimated flapping signals to decrease significantly, while the FDEEs were only slightly degraded, as indicated by the purple traces. Conventionally filtered flapping signals degraded to equivalent SNR levels as the estimated during faults but, conventionally filtered flapping had significantly higher FDEE and time delay. Figure 9 shows the commanded longitudinal actuator activity for the family of optimized KF solutions, where the purple and red traces show the estimated flapping commanded actuator activity with and without synthetically injected spikes, respectively. Similar results were found in the lateral axis.

When the laser sensor system is working properly, the commanded actuator activity lies well below the saturation limit. Injecting sensor faults reveals that the optimized KF solutions have

different degrees of sensitivity. Kalman filter designs with FDEE above 90 are tolerant to sensor failures but, designs with lower FDEEs rely too heavily on measurement data, and would saturate the commanded actuator. Notably, filtered flapping with faults results in comparable or higher actuator activity to the estimated flapping but, the filtered flapping has significantly higher FDEE.

Selected from the family of optimized KF designs, KFb with a FDEE of 60, which relies more heavily on the sensor measurements and acting like a slower, lower gain estimator compared to KFa, which relies less on sensor measurements and more on the model with a FDEE of 120. These designs are indicated in Figure 7 - Figure 9 circled with dotted red traces. Based on linear environment testing, KFa was more robust to faults as indicated by less severe actuator response to faults, whereas KFb better represents the actual flapping motions as indicated by low FDEE.

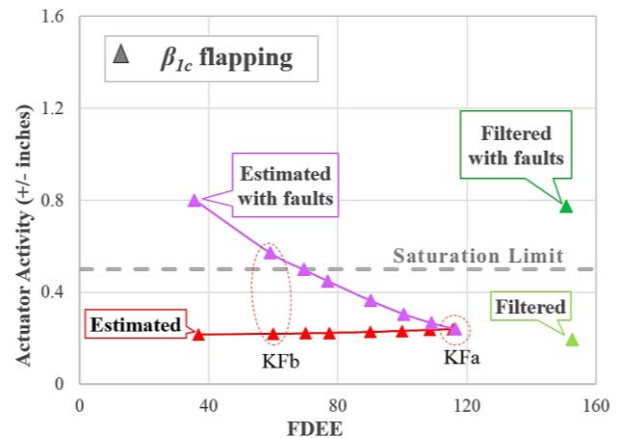


Figure 9. Longitudinal actuator activity and FDEE trade-off.

EXPLICIT RSF CONTROL LAWS DESIGN AND OPTIMIZATION WITH KALMAN FILTER

The effectiveness of two optimized KF designs integrated with the eRSF controls system in Reference [1] was evaluated in linear analysis. The original eRSF controls system uses conventionally filtered flapping signals for RSF. To integrate the Kalman filter designs with the eRSF control laws, the estimated flapping signals from the Kalman filter were exchanged with the conventionally filtered flapping signals in the eRSF control laws, as shown

in Figure 10. Based on the KF design optimization, the estimated flapping signals had less time delay than conventionally filtered flapping signals, providing phase lead. The eRSF with KF designs had higher phase margins, which indicated that eRSF control gains could be re-optimized to utilize this lead to gain tighter tracking performance. Before re-optimizing the KF designs in CONDUIT[®], the estimated flapping signals were verified against raw flapping signals. Explicit rotor-state feedback control gains were re-optimized to provide

maximum disturbance rejection bandwidth via the design margin optimization technique [27], while maintaining desired stability margins, Level 1 handling qualities metrics, and minimizing actuator RMS. An example of the control system is depicted in Figure 10, for the lateral axis. The eRSF with KFb design (lower FDEE) was optimized to a slightly better overall performance index than the KFa design. As indicated in Table 3, the change in control gains of eRSF with KFb design was more evenly distributed, whereas the optimization of KFa had

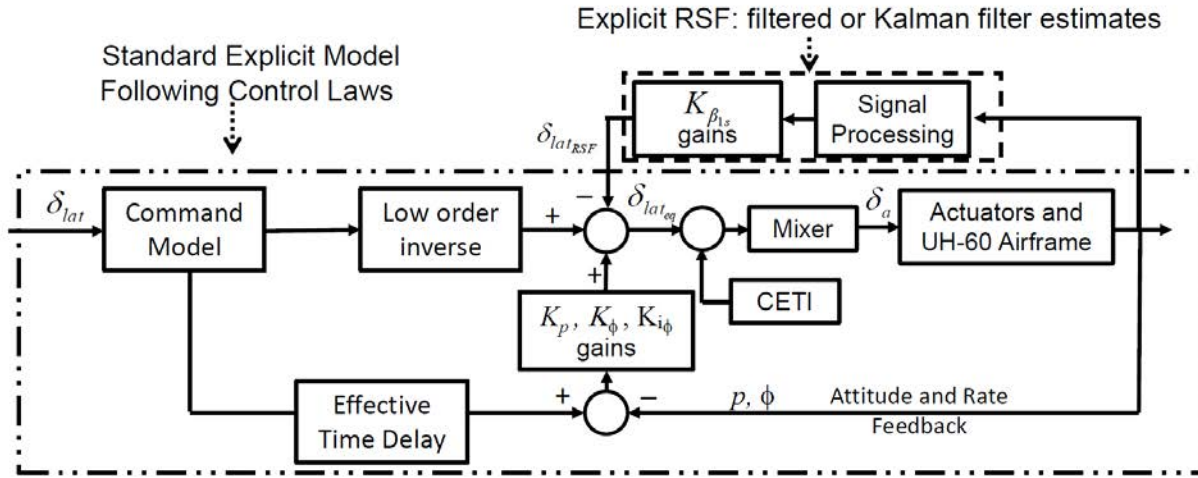


Figure 10. Explicit model following architecture with rotor-state feedback (lateral-axis).

Table 3. Longitudinal and lateral axes optimized feedback gains with Kalman filter.

	eRSF	eRSF with KFa	% Change	eRSF with KFb	% Change
RSF Gains					
$K_{\beta_{1s}}$	10.068	11.631	15.52%	12.799	27.13%
$K_{\beta_{1c}}$	5.985	10.832	81.00%	7.461	24.67%
Inner Loop Gains					
K_p	3.484	3.951	13.41%	3.913	12.32%
K_ϕ	12.776	14.249	11.53%	14.379	12.55%
K_q	8.674	10.984	26.63%	9.923	14.40%
K_θ	11.708	18.647	59.27%	14.489	23.75%

Table 4. Re-optimized lateral control system design characteristics with Kalman filter.

	Gain Margin (dB)	Phase Margin (deg)	Crossover ω_c (rad/s)	Attitude DRB $\omega_{DRB} \phi$ (rad/s)	Actuator RMS (inches)	Actuator rate RMS (inches/s)
eRSF	7.13	63.16	4.65	1.28	0.0458	2.22
eRSF with KFa	10.54	61.64	4.85	1.32	0.0433	1.99
(% Change from eRSF)	(+47.77%)	(-2.42%)	(+4.44%)	(+2.91%)	(-5.31%)	(-10.47%)
eRSF with KFb	8.97	61.38	4.92	1.34	0.0442	2.10
(% Change from eRSF)	(+25.71%)	(-2.83%)	(+5.90%)	(+4.35%)	(-3.40%)	(-5.27%)

Table 5. Re-optimized longitudinal control system design characteristics with Kalman filter.

	Gain Margin (dB)	Phase Margin (deg)	Crossover ω_c (rad/s)	Attitude DRB $\omega_{DRB \theta}$ (rad/s)	Actuator RMS (inches)	Actuator rate RMS (inches/s)
eRSF	11.45	58.21	3.03	0.74	0.0509	3.31
eRSF with KF _a (% Change from eRSF)	21.79 (+90.31%)	59.97 (+3.03%)	3.27 (+8.00%)	0.89 (+20.85%)	0.0461 (-9.40%)	3.02 (-8.59%)
eRSF with KF _b (% Change from eRSF)	20.28 (+77.09%)	56.99 (-2.10%)	3.21 (+5.86%)	0.79 (+7.36%)	0.0482 (-5.31%)	3.13 (-5.45%)

larger increases in the longitudinal control gains. Results of the optimization for the lateral and longitudinal control axes are shown in Table 4 and Table 5. Increased control gains of the eRSF control system resulted in improvements in disturbance rejection bandwidth, crossover frequency, with reduced actuator RMS, and actuator rate RMS in turbulence. Large improvements are seen in the longitudinal axis.

The analysis indicates that improvements in disturbance rejection bandwidth for both explicit rotor-state feedback with Kalman filters are in the range of 2-4% for the lateral axis, and 7-21% for the longitudinal axis. The actuator RMS, actuator rate RMS, and crossover frequencies were also increased by similar amounts for both the eRSF with Kalman filter systems, while maintaining gain margins greater than 7 dB and phase margin over 60 deg.

VALIDATION OF NONLINEAR SIMULATION MODEL

Validation was performed in the frequency domain using the nonlinear GENHEL simulation model. The validation of the nonlinear simulation model ensured that the characteristics designed for in the linear analysis were applicable to the higher fidelity nonlinear blade element model simulation of the UH-60 GENHEL [25]. The linear CONDUIT[®] model broken-loop responses with Kalman filter designs incorporated were simulated in position hold mode, and extracted from CONDUIT[®] with the loop of interest broken at the mixer during automated broken-loop sweeps. The broken-loop flapping responses were generated from the nonlinear simulation with automated frequency sweeps input at the mixer and the frequency response was calculated from input/output on either side of the sweep. The nonlinear and linear analyzes were compared in the frequency domain using

CIFER[®] software [12] to calculate the nonlinear response. An example comparison is given in Figure 11, where linear analysis and nonlinear model are in agreement around the crossover frequency (1-9 rad/s), indicating the linear model provided acceptable predictive accuracy. Closed-loop validation was performed in a similar fashion for the lateral and longitudinal axes, as shown in Figure 12.

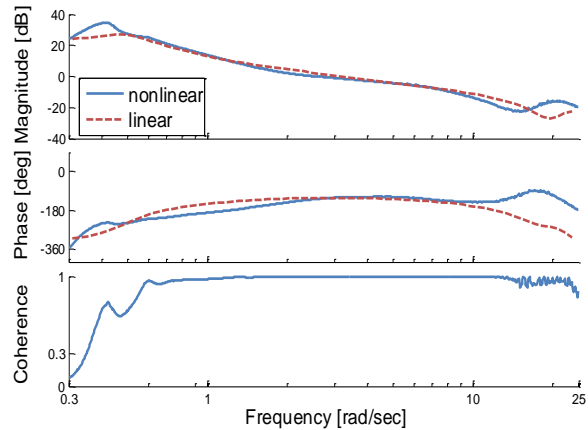


Figure 11. Longitudinal broken-loop response validation for Kalman filter estimated flapping.

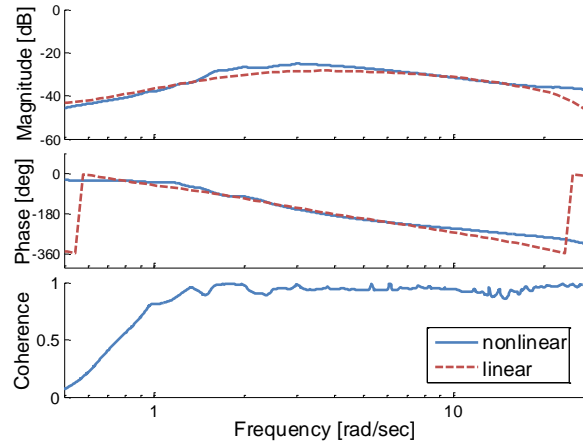


Figure 12. Closed-loop validation of Kalman filter longitudinal flapping β_{1c}/δ_{lon} eq.

Based on these broken-loop and closed-loop responses comparisons, good agreement between the linear and nonlinear models was achieved and validation was sufficiently accurate in all axes.

SIMULATION OF EXPLICIT RSF WITH KALMAN FILTER IN NONLINEAR ENVIRONMENT

Validation of the nonlinear Kalman filter designs led to desktop simulation testing and later limited piloted simulation. Nonlinear environment testing was divided into three cases, presented in Table 6. For case 1, the robustness to faults of the eRSF with KFs were tested. The original eRSF gains

qualities and performance differences between the original eRSF and eRSF with increased gains, piloted evaluations were performed in the Aeroflightdynamics Directorate (AFDD) fixed base simulator, shown in Figure 13.

Although the simulator has a side-stick, instead of a cyclic, it was considered to be sufficient for evaluation of relative effectiveness of the different eRSF designs. The control laws were flown by Marcos Berrios, an operational Air Force pilot with 1000 hours of flight time. The ADS-33E precision hovering turn maneuver [23] was performed for each configuration with moderate turbulence. A hovering turn MTE requires the pilot

Table 6. Simulation tests and test conditions.

Case	Test Designs	Atmosphere Condition	Faults	Evaluation/Purpose
1	eRSF KFa original gains KFb original gains	Calm winds	Opposing blade doublets & spikes	Desktop sim, robustness to faults, actuator activity
2	eRSF KFa optimized gains KFb optimized gains	Moderate Turbulence	None	Piloted sim, DRB performance
3	eRSF KFa optimized gains KFb optimized gains	Moderate Turbulence	Opposing blade doublets & spikes	Piloted sim, DRB performance, pilot comments

were used to expose the impact/difference that the KF made during blade sensor faults. In case 2, the eRSF and eRSF with KFs and re-optimized gains was tested to show the impact that increased gains had on performance. In case 3, comparison of the original eRSF to the eRSF designs with KFs and re-optimized gains was tested for overall advantage of implementing the KF for blade flapping.

Desktop simulation was sufficient for testing robustness to blade faults. To assess the handling

to complete a 180 deg turn to a stabilized hover within a 15 sec window, while maintaining the longitudinal and lateral position within 3 ft of the initiation point on the ground [23]. For simulation of turbulence, the CETI turbulence model was used because it was shown to accurately predict rotor flapping motion in light turbulence for eRSF [2]. The pilot repeated each configuration a minimum of three times and in many cases repeated the maneuver and compared it with the original eRSF control laws.



Figure 13. AFDD fixed base simulator.

Case 1: Robustness to faults

To test robustness in the nonlinear desktop simulation, faults were injected to the individual (rotating blade) flapping signals and the body frame lateral and longitudinal flapping responses used for eRSF were observed. Faults were synthetically created based on observation of over 40 flight records. The worst case scenarios were used to model these failures. A total blade signal failure was very unlikely because individual blade flapping signals are measured using individual flap, lead-lag, and pitch measurements for each of the four blades. For the purposes of testing the robustness of the

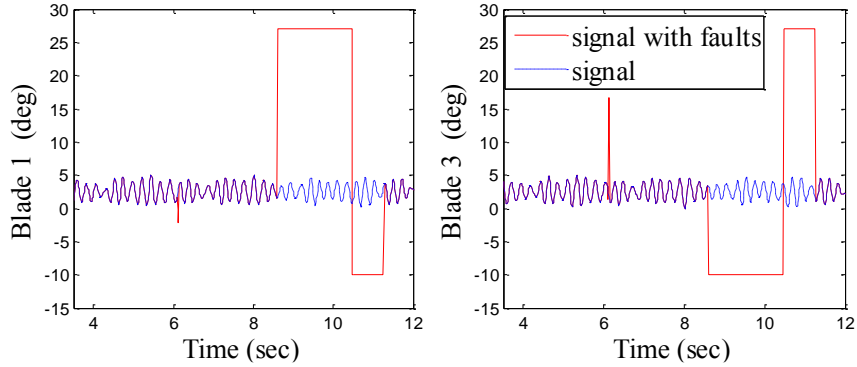


Figure 14. Faults injected in opposite directions on opposing blades 1 and 3.

Kalman filter designs, the worst case for lateral and longitudinal rotor flapping faults were tested. This would occur if opposing blades had opposing faults of maximum values injected simultaneously. The most severe cases included faults with spikes at random magnitudes and doublet-hardovers/dropouts at the most severe magnitudes, which are shown in Figure 14 at 6 seconds and 8 seconds respectively. The conventionally filtered method reacted unfavorably to injected faults whereas the Kalman filter estimated flapping has the capacity to mitigate

had marginally better performance during faults compared to KFb, likely due to the fact that KFa relies less on sensor measurements.

Case 2: Disturbance rejection in turbulence

In addition to handling faulty measurement data, the KF estimated flapping signals provide phase lead, which enabled modest increases to feedback gains. Increased gains resulted in improvements in disturbance rejection bandwidth, which had a significant effect on position

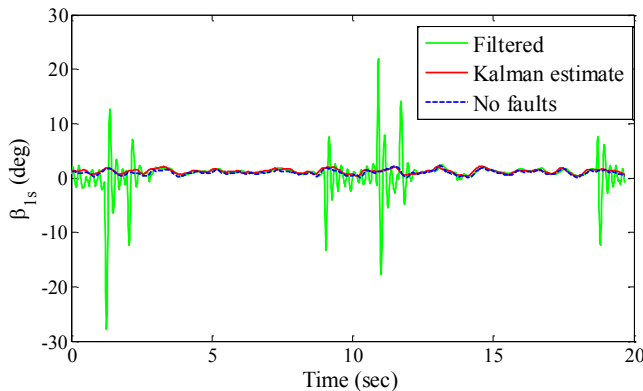


Figure 15. Comparison of eRSF current filtered lateral flapping and Kalman estimated lateral flapping during faults.

faults, as shown in Figure 15. Two KF designs were evaluated to compare how a higher gain estimator, that deweights the sensor measurements, would behave to faults. Actuator RMS results show that both KF designs are sufficiently robust to faults, while the conventionally filtered eRSF is not. With the original eRSF gains, the two KF designs show similar improvements in actuator RMS, SNR, and flapping error in both axes. Recall that KFa relies more on the model and KFb relies more on sensor measurements. Table 7 shows that as expected, KFa

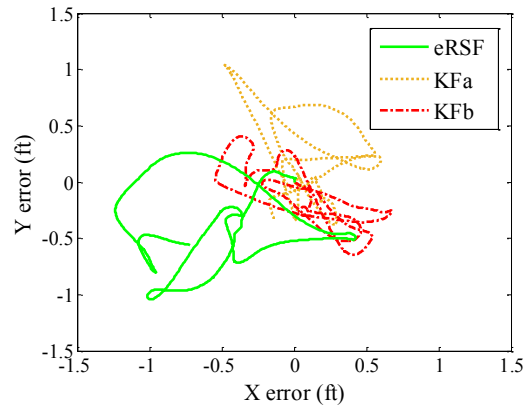


Figure 16. Comparison of controller position error during Hovering Turn MTE with turbulence.

maintenance. Decreases in position and attitude error, or difference between the actual and commanded position and attitude are presented in Table 8. Larger improvements in tracking were observed in pitch than roll. As shown in Figure 16, both eRSF with Kalman filter designs had improved tracking compared to the eRSF with conventionally filtered flapping. The pilot found that there was “very little difference between the two configurations KFa and KFb.” Because the re-

Table 7. Robustness to faults in Hover with original eRSF gains.

Configuration	Lat. Actuator RMS (inches)	Lon. Actuator RMS (inches)	SNR β_{1s}	SNR β_{1c}	$\sigma(\beta_{1s \text{ error}})$ (deg)	$\sigma(\beta_{1c \text{ error}})$ (deg)
eRSF	1.376	0.276	9.290	7.076	6.771	7.650
eRSF with KFa (% Change from eRSF)	1.371 (-0.391%)	0.262 (-4.848%)	40.378 (+335%)	32.189 (+355%)	0.684 (-89.90%)	0.132 (-98.28%)
eRSF with KFb (% Change from eRSF)	1.372 (-0.315%)	0.264 (-4.265%)	40.036 (+331%)	32.136 (+354%)	0.549 (-91.89%)	0.115 (-98.50%)

Table 8. Hovering Turn in turbulence with re-optimized gains.

Configuration	Lon. Track $\sigma(X_{err})$ (ft)	Lat. Track $\sigma(Y_{err})$ (ft)	Roll Att. Track $\sigma(\phi_{err})$ (deg)	Pitch Att. Track $\sigma(\theta_{err})$ (deg)
eRSF	1.562	1.061	5.076	3.701
eRSF with KFa (% Change from eRSF)	1.179 (-24.53%)	0.933 (-12.12%)	4.075 (-19.72%)	3.092 (-16.43%)
eRSF with KFb (% Change from eRSF)	1.181 (-24.37%)	1.048 (-1.21%)	3.963 (-21.93%)	3.319 (-10.31%)

Table 9. Hovering Turn in turbulence with re-optimized gains and faults.

Configuration	Lon. Track $\sigma(X_{err})$ (ft)	Lat. Track $\sigma(Y_{err})$ (ft)	Roll Att. $\sigma(\phi_{err})$ (deg)	Pitch Att. $\sigma(\theta_{err})$ (deg)	$\sigma(\beta_{1s \text{ err}})$ (deg)	$\sigma(\beta_{1c \text{ err}})$ (deg)
eRSF	1.690	1.540	5.634	4.179	10.60	16.75
eRSF with KFa (% Change from eRSF)	1.313 (-22.32%)	1.172 (-23.88%)	5.586 (-0.85%)	3.142 (-24.82%)	1.280 (-87.93%)	1.483 (-91.14%)
eRSF with KFb (% Change from eRSF)	0.999 (-40.87%)	0.844 (-45.23%)	3.877 (-31.19%)	2.846 (-31.90%)	0.725 (-93.16%)	1.314 (-92.16%)

optimized eRSF gains were similar between the two KF designs, it was not surprising that their tracking performance was similar.

Case 3: Disturbance rejection in turbulence with faults

Finally, the original eRSF and the re-optimized eRSF with KF designs were compared in turbulence with faults. Faults were injected throughout the maneuver without the pilot’s knowledge. As shown in Figure 17, the eRSF with KF designs both demonstrate significantly improved position maintenance compared to eRSF with conventional filters. Table 9 shows that eRSF with KF designs achieved even greater improvements in disturbance rejection during position maintenance during faults than the previous eRSF design. Pilot feedback after the Hovering Turn maneuvers during turbulence with faults matched this conclusion;

according to the pilot, he would virtually not experience faults, whereas with the original eRSF, faults were evident, “the behavior of eRSF without KFs is less smooth and more erratic, less predictable

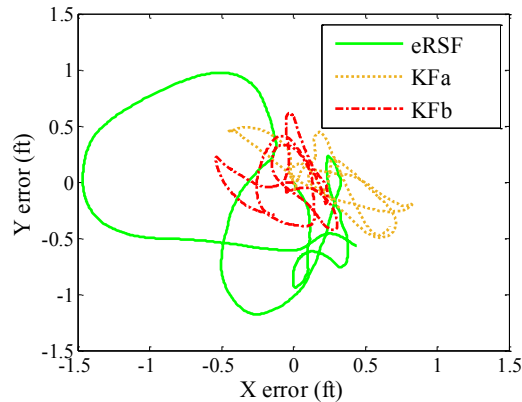


Figure 17. Comparison of controller position error during Hovering Turn MTE with turbulence and faults.

during faults.” When faults were injected, the performance between the two Kalman filter designs was more evident. From Table 9, KFb was the better design option. The eRSF with KFb, more reliant on sensor measurements, likely had higher disturbance rejection capabilities during faults because overall it also had slightly higher eRSF gains.

Final selection of the level of aggression of the KF design from the family of optimized KFs should be based on pilot preference along with the expected regularity or likelihood of occurrence and severity of faults to the system. Overall, both Kalman filter designs were robust to faults and produced flapping estimates with no time delay. The key advantage to the KFb is that the eRSF could be optimized to higher gains, which resulted in better tracking performance.

CONCLUSIONS

This study evaluated optimizing the process covariance matrix of a Kalman filter (KF) using frequency domain specifications. A family of KF designs for estimation of lateral and longitudinal rotor blade flapping signals were designed to minimize measurement noise, sensor error, and eliminate time delay. These estimated KF flapping signals were fed back in the explicit rotor-state feedback (eRSF) control laws. The eRSF control gains were re-optimized in CONDUIT[®] using the estimated KF flapping signals in place of conventionally filtered flapping signals. This led to a system more robust to rotor blade sensor faults and increased handling qualities, while maintaining desired stability margins. This optimization based methodology is generic in nature, so the KF could be useful for any measurement system that measures blade motion. Conclusions from this research are:

1. Optimization of the process noise covariance matrix based on frequency domain specifications allowed the KF to be tuned to a customized performance index. This increased transparency of tuning for desired behaviors, in this case maintaining low and mid-range frequency content and filtering high frequency signal content.
2. Using a KF to estimate blade flapping measurements provides sensor fault tolerant robustness and improved signal quality. Both KF designs could mitigate worst-case

rotor blade sensor fault scenarios, which included simultaneous spikes and dropouts on all four blades. The KF estimated signals had increased signal-to-noise ratio by a factor of 3.5 and improved time delay from a lag of approximately 0.05 seconds to a lead of 0.04 seconds.

3. Explicit rotor-state feedback utilizing KF estimated flapping provide improvements in disturbance rejection and crossover frequency, resulted in improved tracking performance, while maintaining sufficient stability margins. Tracking performance was improved during the Hovering Turn MTE during moderate turbulence, on the order of 15% without blade faults and on the order of 40% when faults were present.

REFERENCES

- [1] C. M. Ivler, "Development and Comparison of Explicit and Implicit Rotor-State Feedback Control System for a Fly-by-Wire UH-60," in *American Helicopter Society Handling Qualities Specialists' Meeting Proceedings*, Huntsville, AL, February 19-20, 2014.
- [2] C. M. Ivler, H. M. Mansur, Z. G. Morford, K. Kalinowski and M. E. Knapp, "Flight Test of Explicit and Implicit Rotor-State Feedback Fly-By-Wire Control Laws," in *American Helicopter Society 72nd Annual Forum*, West Palm Beach, FL, May 17-19, 2016.
- [3] S. J. Briczinski, "Analytical Investigation of Gust Suppression Techniques for the CH-53 Helicopter," NASA CR-145031, Stratford, 1976.
- [4] J. F. Horn , W. Guo and G. T. Ozdemir, "Use of Rotor State Feedback to Improve Closed-Loop Stability and Handling Qualities," *Journal of the American Helicopter Society*, vol. 57, no. 2, pp. 1-10, April 2012.
- [5] E. Morales III and et. al, "Flight Research Qualification of the Army/NASA RASCAL Variable Stability Helicopter," in *American Helicopter Society 58th Annual Forum Proceedings*, Montreal, Canada, June 2002.
- [6] J. Fletcher and M. Tischler, "Improving Helicopter Flight Mechanics Models with Laser

- Measurements of Blade Flapping," in *AHS 53rd Annual Forum*, Virginia Beach, VA, April 1997.
- [7] P. Cordisco and e. al., "Developing a Novel Contactless Sensor for Helicopter Rotor State Measurements," in *36th European Telemetry and Test Conference*, Nuremberg, May 2016.
- [8] J. Snider, "Future Directions in Tactile Vertical Lift," American Helicopter Society, Washington D.C., April, 2010.
- [9] R. J. McKillip and J. Keller, "Data-Driven Modeling for Rotor State Feedback Simulation," in *67th AHS Forum*, Virginia Beach, VA, May 2011.
- [10] R. W. Du Val, "Use of multiblade sensors for on-line rotor tip-path plane estimation," *American Helicopter Society*, vol. 25, pp. 13-21, Oct 1, 1980.
- [11] W. Johnson, *Helicopter Theory*, New York: Dover Publications, Inc., 1980.
- [12] M. B. Tischler and R. K. Remple, *Aircraft and Rotorcraft System Identification: Engineering Methods with Flight Test Examples*, Reston, VA: American Institute of Aeronautics and Astronautics, Inc., 2012, pp. 100-200.
- [13] J. W. Fletcher, R. T. N. Chen and E. Strasilla, "State Estimation of Main Rotor Flap and Lead-Lag Using Accelerometers and Laser Transducers on the RASCAL UH-60 Helicopter," 34th AIAA Aerospace Sciences Meeting (Atmospheric Flight Mechanics), Reno, NV, January 15-18, 1996.
- [14] O. Bruhis, M. Idan and R. W. DuVal, "Estimation of UH-60 Blade Aerodynamic Loads and Rotor Impedance using Generalized Strain Pattern / Kalman Filter Approach," in *AHS 46th Annual Forum*, Washington, D.C., May 21-23, 1990.
- [15] S. J. Briczinski and D. E. Cooper, "Flight Investigation of Rotor/Vehicle State Feedback," NASA-132546, Stratford, 1975.
- [16] R. E. Kalman and R. S. Bucy, "New results in linear filtering and prediction theory," *Journal of Basic Engineering*, vol. 83, no. 3, pp. 95-108, 1961.
- [17] S. Formentin and S. Bittanti, "An insight into noise covariance estimation for Kalman filter design," in *The International Federation of Automatic Control*, Cape Town, 2014.
- [18] G. Welch and G. Bishop, "An Introduction to the Kalman Filter," University of North Carolina at Chapel Hill, Chapel Hill, NC, USA, 2006.
- [19] A. Solonen, J. Hakkarainen, A. Ilin, M. Abbas and A. Bibov, "Estimating model error covariance matrix parameters in extended Kalman filtering," *Nonlinear Processes in Geophysics*, vol. 21, pp. 919-927, 1 September 2014.
- [20] B. M. Akesson, J. B. Jorgensen, N. K. Poulsen and S. Jorgensen, "A generalized autocovariance least-squares method for kalman filter tuning," *Journal of Process control*, vol. 18, no. 7, pp. 769-779, 2008.
- [21] P. Matisko and V. Havlena, "Noise covariance estimation for kalman filter tuning using bayesian approach and monte carlo," *International Journal of Adaptive Control and Signal Processing*, vol. 27, no. 11, pp. 957-973, 2013.
- [22] V. H. Knight, W. S. J. Haywood and M. L. J. Williams, "A Rotor-mounted Digital Instrumentation System for Helicopter Blade Flight Research Measurements," NASA Technical Paper 1146, Langley Research Center, Hampton, VA, April 1978.
- [23] Anon, *Aeronautical design Standard, Handling Quality Requirements for Military Rotorcraft*, ADS-33E-PRF, U.S. Army Aviation and Missile Command (USAAMCOM), 2000.
- [24] R. M. Kufeld and P. S. Loschke, "UH-60A Airloads Program: Status and Plans," in *AIAA/AHS/ASEE Aircraft Design System and Operations Meeting*, Baltimore, MD, September 1991.
- [25] J. Howlett, "UH-60 Black Hawk Engineering Simulation Program: Volume 1 -Mathematical Model," 1981.
- [26] F. D. Kim, R. Celi and M. B. Tischler, "High Order State Space Simulation Model of Helicopter Flight Mechanics," *Journal of the American Helicopter Society*, vol. 38, 1993.
- [27] M. B. Tischler, T. Berger, C. M. Ivler, M. H. Mansur, K. K. Cheung and J. Y. and Soong, *Practical Methods for Aircraft and Rotorcraft Flight Control Design: An Optimization-Based Approach*, Reston, VA: American Institute of Aeronautics and Astronautics, Inc., 2017.